J Mater Sci: Mater Electron (2020) 31:19613–19622

Enhanced photocatalytic activity of ternary g-C_3N_4/$NaTaO_3$/biomass carbon composite photocatalysts under visible-light radiation

Shengze Li[1], Jinlong Liao[1], Yubin Dong[1], Yaqin Fu[1], and Yaofeng Zhu[1,*]

[1] *Key Laboratory of Advanced Textile Materials and Manufacturing Technology Ministry of Education, Zhejiang Sci-Tech University, Hangzhou 310018, Zhejiang, China*

Received: 7 May 2020
Accepted: 11 September 2020
Published online: 24 September 2020

ABSTRACT

Highly efficient visible-light-responsive ternary graphitic carbon nitride (g-C_3N_4)/$NaTaO_3$/biomass carbon (BM-C) photocatalysts with different g-C_3N_4 amounts were prepared via a solvothermal method combined with a high-temperature sintering method. Herein, the crystal structure and morphology of g-C_3N_4/$NaTaO_3$/BM-C are investigated in detail. The light-response characteristics of g-C_3N_4/$NaTaO_3$/BM-C composites are effectively extended into the visible-light region. Compared with $NaTaO_3$/BM-C and g-C_3N_4/$NaTaO_3$, the g-C_3N_4/$NaTaO_3$/BM-C composite showed high visible-light catalytic performance when the mass ratio of melamine (the g-C_3N_4 precursor) to binary $NaTaO_3$/BM-C is 4:1, and the degradation extent of 95.85% for Rhodamine B can be reached in 60 min under visible-light irradiation. In addition, the photocatalytic mechanism showed that the enhanced photocatalytic activity of the composite may be attributed to the introduction of g-C_3N_4, which expanded the visible-light response range and the formation and effect of a good synergistic effect of BM-C and various components. This work provides useful insights for promoting the practical process of sodium tantalate photocatalytic materials.

1 Introduction

For decades, with the rapid growth of the world economy, the energy crisis and environmental pollution have become ever-increasing problems globally, posing a serious threat to human production and life [1–4]. Semiconductor-based photocatalysis technology is a promising green chemical technique with great potential in wastewater purification [5–10]. Among them, $NaTaO_3$ is particularly attractive due to its nontoxicity, chemical and physical stability, and structural properties [11]. Moreover, $NaTaO_3$ has favorable band-edge potentials and photogenerated electron–hole pair separation because of the large bond angle of Ta–O–Ta, which are primary reasons for higher efficiency [12–14]. However, because of its wide band-gap energy (3.8–4.0 eV), the photocatalytic activity of $NaTaO_3$ is limited to the ultraviolet

Address correspondence to E-mail: yfzhu@zstu.edu.cn

https://doi.org/10.1007/s10854-020-04488-z

(UV) region, which greatly reduces its photocatalytic efficiency and restricts its widespread applications [15, 16].

To remedy the limitation of $NaTaO_3$ and to enhance its visible-light photocatalytic activity, many efforts such as doping with a nonmetal [17, 18], depositing noble metals [19, 20], applying sacrificial [21], and constructing heterojunction photocatalysts [22–24] have been made. Recently, the fabrication of $NaTaO_3$-based heterojunction photocatalysts has attracted ever-increasing attention and is considered a promising method to obtain significant visible-light response [25]. Graphitic carbon nitride (g-C_3N_4), a novel type of semiconductor with a narrow band gap, is widely used in the environment because of its stable, environmentally friendly, and visible-light-responsive performance [26, 27]. However, the visible-light photocatalytic efficiency of g-C_3N_4 is still at a low state due to the fast recombination of photogenerated charge carriers in pure g-C_3N_4 [28–30]. Therefore, fabrication of g-C_3N_4/$NaTaO_3$ heterojunction photocatalysts is proposed because of the well-matched energy-band structure of g-C_3N_4 and $NaTaO_3$, which may enhance the visible-light photocatalytic activity.

Apart from the lack of visible-light response, the application of $NaTaO_3$ is also restricted by the inferior surface adsorption capacity, which affects the photocatalytic efficiency. Carbon materials exhibit superior adsorption capacity and their efficient electron-transfer property has led to them being used as ideal photocatalyst supports [31]. Biomass carbon (BM-C), a type of biomass feedstock-derived carbonaceous material, is highly porous, has good absorption, low cost, and environmental friendliness, which has made it recognized as one of the most promising photocatalyst supporters [32–35]. Meanwhile, it can also efficiently reduce the recombination of photoinduced electrons and holes by accelerating electron transfer from the surface of a photocatalyst [36, 37]. In view of the above, it is clear that the photocatalytic activity of $NaTaO_3$ can be enhanced by a combination with BM-C.

Inspired by the aforementioned insights, a series of g-C_3N_4/$NaTaO_3$/BM-C composite photocatalysts were successfully synthesized using a solvothermal method combined with a high-temperature sintering method. The morphology, structure, and chemical composition of prepared composite photocatalysts were characterized using field emission–scanning electron microscopy (FE–SEM), X-ray powder diffraction, Fourier transform infrared (FT-IR) spectroscopy, X-ray photoelectron spectroscopy, and UV–visible diffuse reflectance spectroscopy. The visible-light photocatalytic performance of the composite photocatalysts was evaluated for the degradation of Rhodamine B (Rh B) under visible-light irradiation. The possible photocatalytic reaction mechanism is also discussed.

2 Experimental section

2.1 Materials

Melamine ($C_3H_6N_6$) used in the experiments was supplied by Tianjin Kemiou Chemical Reagent Co., Ltd. Barium chloride ($TaCl_5$) and ethylene glycol ($C_2H_6O_2$) were brought from Shanghai Macklin Biochemical Technology Co., Ltd. Sodium hydroxide (NaOH) was purchased from Hangzhou Gaojing Fine Chemical Co., Ltd. All chemicals were of analytical grade and used as purchased without further purification. Deionized water was used in all experiments.

2.2 *Preparation of $NaTaO_3$/BM-C composite*

The BM-C was prepared using oxygen-limited temperature-controlled carbonization methods with peanut hull as raw materials. On this basis, 0.25 g BM-C, 0.385 g $TaCl_5$, and 5.0 g NaOH were added to a mixed solution of 40 mL of ethylene glycol and 20 mL of deionized water, and stirred for 30 min. Then, the above mixed solution was transferred to a 100 mL reaction vessel and reacted at 180 °C for 18 h. After the reaction, the product was centrifuged, washed with deionized water to neutrality, and dried in an oven at 80 °C for 12 h to obtain a $NaTaO_3$/BM-C composite photocatalyst.

2.3 *Synthesis of g-C_3N_4/$NaTaO_3$/BM-C composite photocatalyst*

The g-C_3N_4/$NaTaO_3$/BM-C composite photocatalyst was prepared as follows: first, a certain amount of melamine and 0.25 g $NaTaO_3$/BM-C were dispersed into deionized water (10 mL) and stirred for 0.5 h afterward, the mixed solution was dried at 100 °C for

8 h. After that, the dried mixture was calcined in a tube furnace under N_2 at 550 °C for 3 h. Finally, the g-C_3N_4/$NaTaO_3$/BM-C composite photocatalyst was obtained after the calcination process. Samples synthesized with melamine additive content 0.50 g, 0.75 g, 1.00 g, and 1.25 g were denoted as g-C_3N_4/$NaTaO_3$/BM-C-2, g-C_3N_4/$NaTaO_3$/BM-C-3, g-C_3N_4/$NaTaO_3$/BM-C-4, and g-C_3N_4/$NaTaO_3$/BM-C-5.

2.4 Characterization

The morphology of the prepared sample was analyzed using FE–SEM (Hitachi S-4800). The crystal phase structure of the material was confirmed using an X-ray diffractometer (XRD, Bruker AXSD8-Discover) in the 2θ range from 20° to 80°. The FT-IR spectra were recorded in transmission mode from 4000 to 400 cm^{-1} on a Nicolet-5700 FT-IR spectrometer using the standard KBr disk method. The UV–visible absorption of the samples was measured using an ultraviolet–visible spectrometer (UV–vis, CARY-300) in the range of 200–800 nm, using $BaSO_4$ as the reference. The photoluminescence (PL) spectrum was characterized on an X-ray diffraction fluorescence spectroscope (Hitachi, F-7000) with a 300 nm excitation light.

2.5 Photocatalytic activity test

In the photocatalytic degradation experiment, a 350 W xenon lamp with a UV-cutoff filter was used as the visible-light source, and Rh B was used as the target pollutant to evaluate the visible-light catalytic performance of the composite photocatalysts. Before light irradiation, 40 mg of the solid photocatalyst was added to 40 mL of 10 mg/L pollutants and then stirred continuously in the dark for 1 h to ensure an adsorption–desorption equilibrium. Five test tubes were prepared from the same sample to analyze the degradation concentration of the dye at different irradiation times. During photocatalytic processes, the test tube for the sample was periodically withdrawn and centrifuged to separate the photocatalyst from the solution. The absorbance of the solution was measured using a UV–vis spectrophotometer (UH-1901).

3 Results and discussion

The morphology of samples was investigated using FE–SEM. Figure 1 shows the FE–SEM images of BM-C, $NaTaO_3$/BM-C, and g-C_3N_4/$NaTaO_3$/BM-C composite. It can be seen that the BM-C possesses abundant pores and a pore size between 100 nm and 1 μm (Fig. 1a). It can be seen from Fig. 1b that the $NaTaO_3$ particles are uniformly distributed on the surface of the BM-C, and the existence of a large number of pore structures. For the g-C_3N_4/$NaTaO_3$/BM-C composite photocatalysts, it is clearly seen that the composite photocatalysts appear to be aggregated particles containing many smaller crystals that covered the surface of BM-C (Fig. 1c–f).

XRD patterns of the g-C_3N_4/$NaTaO_3$/BM-C samples with various g-C_3N_4 amounts are shown in Fig. 2. The XRD pattern of $NaTaO_3$ can be indexed as an orthorhombic structure according to the JCPDS card (25-0863) [38]. The peaks at 2θ at 22.9°, 32.5°, 40.1°, 46.6°, 52.5°, 57.9°, 68.2°, 73.3°, and 77.8° are attributed to the (020), (121), (220), (202), (222), (321), (242), (303), and (321) crystal planes of $NaTaO_3$, respectively. For bare g-C_3N_4, two main diffraction peaks appear at 13.1 and 28.0°, which correspond to the (100) and (002) crystal planes of g-C_3N_4, respectively (JCPDS No. 87-1526) [39]. It can also be seen that the characteristic peaks of pristine $NaTaO_3$ and g-C_3N_4 are present in the XRD pattern of the g-C_3N_4/$NaTaO_3$/BM-C samples. With increasing content of g-C_3N_4, the intensity of the g-C_3N_4 characteristic diffraction peaks is enhanced. Moreover, the diffraction peaks belonging to $NaTaO_3$ of the g-C_3N_4/$NaTaO_3$/BM-C are clearly weakened, indicating that the g-C_3N_4 loading led to a decrease in crystallinity of $NaTaO_3$ [14]. Compared with $NaTaO_3$/g-C_3N_4, no new peaks are found in $NaTaO_3$/g-C_3N_4/BM-C because the characteristic peaks of BM-C are overlapped by those of $NaTaO_3$ and g-C_3N_4.

FT-IR spectra were used to investigate chemical groups of the samples. Figure 3a shows the FT-IR spectra of g-C_3N_4, $NaTaO_3$/BM-C, and g-C_3N_4/$NaTaO_3$/BM-C. In the FT-IR spectrum of g-C_3N_4, the peak at 815 cm^{-1} is assigned to the stretching vibration of the triazine units [40], the peaks at around 1200–1700 cm^{-1} are attributable to aromatic C–N stretching and C=N stretching vibration modes [41]. The peak at 2900 cm^{-1} is related to the N–H stretching vibrations [42]. As for $NaTaO_3$/BM-C, a strong absorption peak around 650 cm^{-1} is assigned to Ta–O

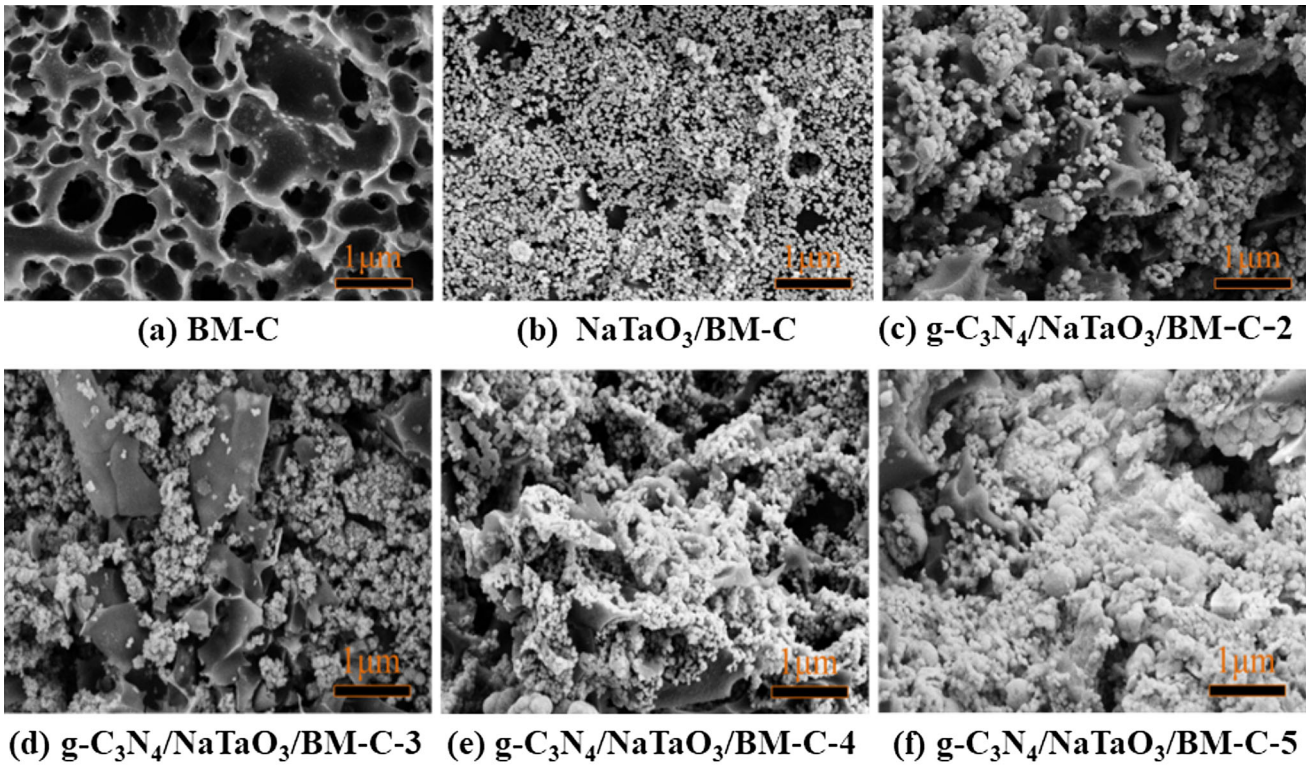

Fig. 1 SEM images of BM-C (**a**), $NaTaO_3$/BM-C (**b**), g-C_3N_4/$NaTaO_3$/BM-C-2 (**c**), g-C_3N_4/$NaTaO_3$/BM-C-3 (**d**), g-C_3N_4/$NaTaO_3$/BM-C-4 (**e**), and g-C_3N_4/$NaTaO_3$/BM-C-5 (**f**)

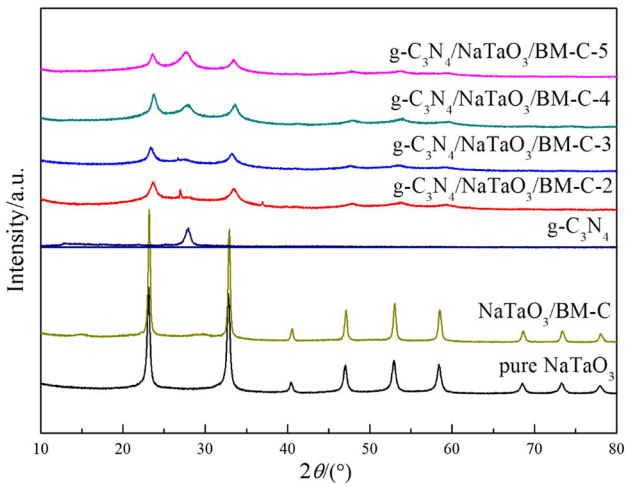

Fig. 2 XRD patterns of the g-C_3N_4, $NaTaO_3$/BM-C and g-C_3N_4/$NaTaO_3$/BM-C composites

stretching and Ta–O–Ta bridging stretching modes [38]. The peak at 3400 cm^{-1} is observed due to adsorbed H_2O molecules on the surface of the sample [43]. All characteristic peaks of $NaTaO_3$ and g-C_3N_4 are observed in g-C_3N_4/$NaTaO_3$/BM-C hybrid nanocomposite samples, which confirms the construction of ternary composites. In addition, it is seen in Fig. 3b that the characteristic absorption peaks belonging to g-C_3N_4 are enhanced with the increase of g-C_3N_4 content.

XPS has been performed to analyze the chemical composition and the chemical state of the resulting samples. The survey spectrum of g-C_3N_4/$NaTaO_3$/BM-C-4 exhibits distinct peaks of Ta, Na, O, C, and N. In Fig. 4b, the high-resolution Ta 4f spectrum can be deconvoluted into two peaks at binding energies of 26.6 eV and 28.4 eV, corresponding to the characteristic peaks of Ta $4f_{5/2}$ and Ta $4f_{7/2}$, respectively, from $NaTaO_3$ [43]. The C 1 s spectrum of g-C_3N_4/BM-C/$NaTaO_3$-4 is shown in Fig. 4c. The wide peak of C 1 s can be fitted to two distinct peaks at binding energies of 288.4 and 284.8 eV, ascribed to the C–N–C bond and C–C bond, respectively [42]. It can be seen from Fig. 4d that the *N* 1 s spectrum of g-C_3N_4/BM-C/$NaTaO_3$-4 exhibits peaks at binding energies of 398.8, 400.5, and 404.7 eV, which are related to sp^2-hybridized N atoms to C (C=N–C), tertiary nitrogen (N–$(C)_3$) groups, and the charging effects or positive charge localization in the heterocycles, respectively [44].

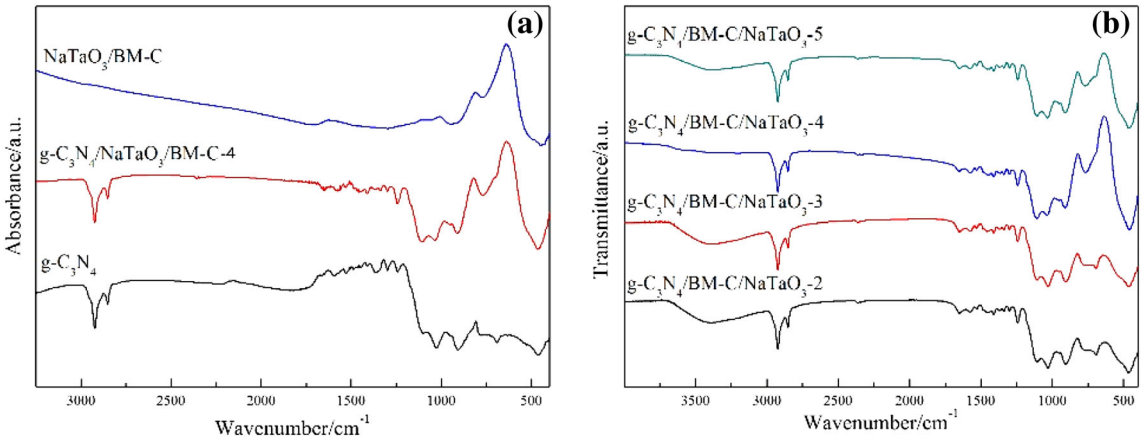

Fig. 3 FT-IR spectra of **a** g-C_3N_4, $NaTaO_3$/BM-C, g-C_3N_4/$NaTaO_3$/BM-C composites and **b** g-C_3N_4/$NaTaO_3$/BM-C composites with different weight of g-C_3N_4

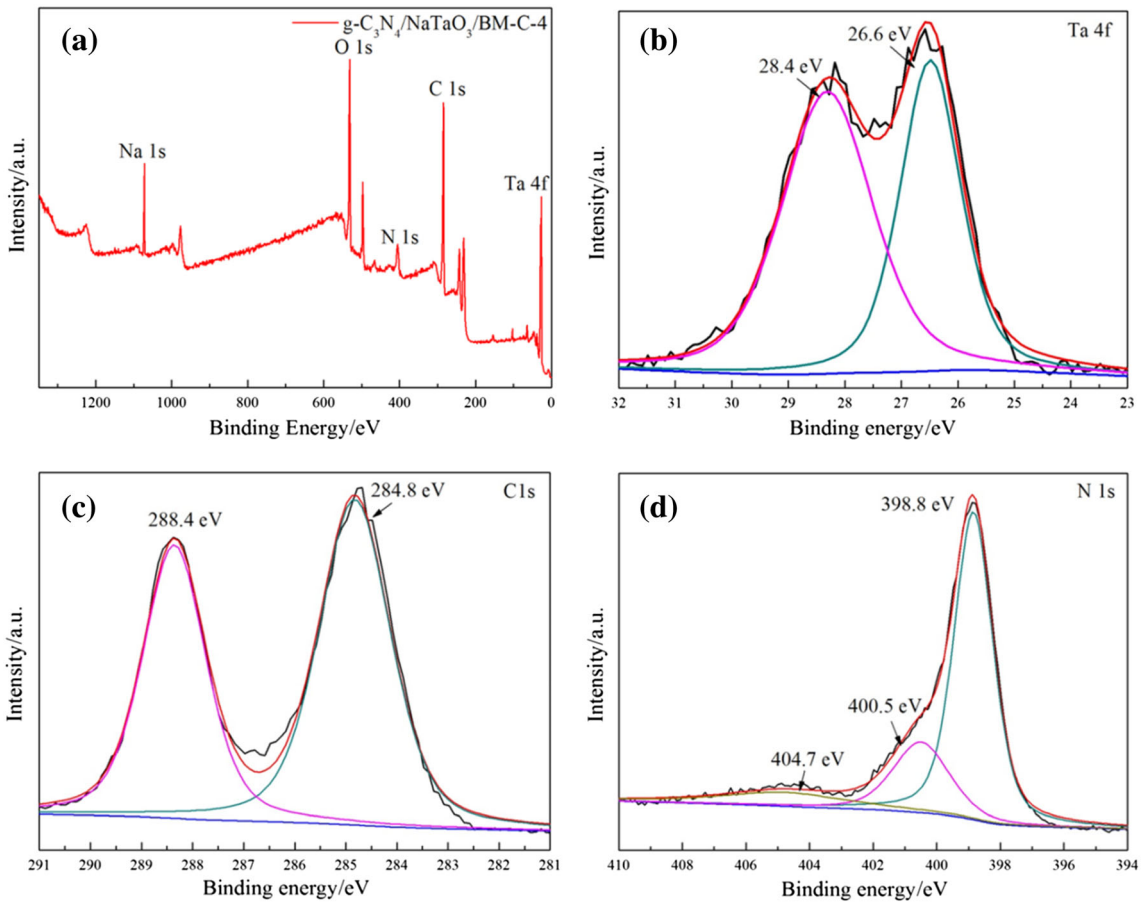

Fig. 4 XPS surveys of g-C_3N_4/$NaTaO_3$/BM-C-4 (**a**), Ta4f spectra (**b**), C1s spectra (**c**), and N1s spectra (**d**)

The light-absorption properties of $NaTaO_3$, $NaTaO_3$/BM-C, and g-C_3N_4/$NaTaO_3$/BM-C were investigated using UV–vis diffuse reflectance spectroscopy (as shown in Fig. 5a). Although the pure $NaTaO_3$ sample exhibits obvious absorption property in the UV-light region, it shows almost no absorbance of visible light due to its large band gap. BM-C exhibits superior adsorption capacity and efficient electron transfer and has been used as an ideal photocatalyst support. After coupling BM-C and

$NaTaO_3$, it is noted that the binary catalyst shows distinct intense absorption in the visible-light region in contrast to pure $NaTaO_3$. Moreover, with the introduction of g-C_3N_4, the ternary catalyst shows an expanded visible-light-absorption range compared with that of $NaTaO_3$/BM-C. It can be seen that the absorption edges are at around 310 and 475 nm in the spectrum. Furthermore, the characteristic absorption band edge of the ternary catalyst extends gradually with the increased proportion of g-C_3N_4.

In addition, the band-gap energies (E_g) of various as-prepared photocatalysts were determined using the following equation:

$$(\alpha h\nu)^2 = A(h\nu - E_g), \quad (1)$$

where $h\nu$, α, and A represent the photon energy, the absorption coefficient, and a constant, respectively. The band gaps of $NaTaO_3$ and g-C_3N_4 are, respectively, calculated to be 3.54 eV and 2.49 eV, as shown in Fig. 6. The valence band and conduction band (CB) potential position of the g-C_3N_4/$NaTaO_3$/BM-C composite is estimated combining the DRS results with the following formulas:

$$E_{VB} = \chi - E^e + 0.5E_g, \quad (2)$$

$$E_{CB} = E_{VB} - E_g, \quad (3)$$

where E_{VB}, E_{CB}, and χ denote the valence band potential, the CB potential, and the electronegativity. The electronegativity values of sodium tantalate and carbon nitride are 5.497 and 4.730 eV [45], respectively. E^e is a hydrogen potential of 4.500 eV, where NHE represents the electrode potential of a standard hydrogen electrode. As a result, the valence potential

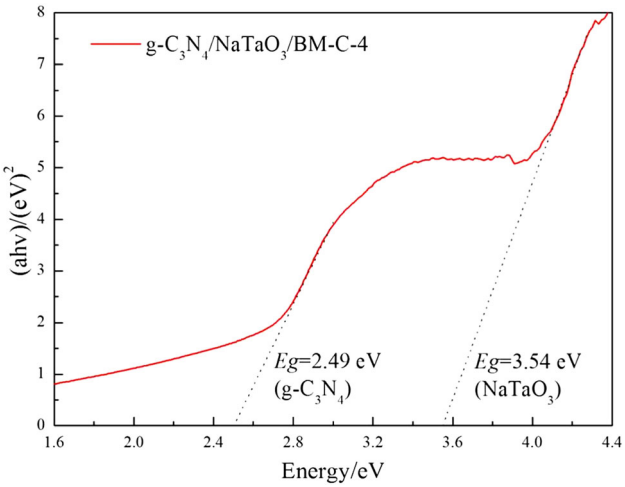

Fig. 6 Plot of $(\alpha h\nu)^2$ versus energy hν for the Eg of g-C_3N_4/$NaTaO_3$/BM-C-4

can be calculated to be 2.767 eV for sodium tantalate ($NaTaO_3$) and 1.475 eV for carbon nitride (g-C_3N_4), while the CB potential of those in the composites can be calculated to be − 0.773 eV and −1.015 eV, respectively. Room-temperature PL spectroscopy was also performed for the g-C_3N_4/$NaTaO_3$/BM-C. The PL emission spectra of g-C_3N_4/$NaTaO_3$/BM-C photocatalyst are shown in Fig. 5b. In Fig. 5b, an obvious PL signal at ca. 484 nm can be observed. Combining the results of UV–Vis DRS and PL, it can be believed that the heterojunction of g-C_3N_4/$NaTaO_3$ and the addition of biomass carbon may effectively prevent charge recombination, resulting in the enhancement of photocatalytic reactivity [46, 47].

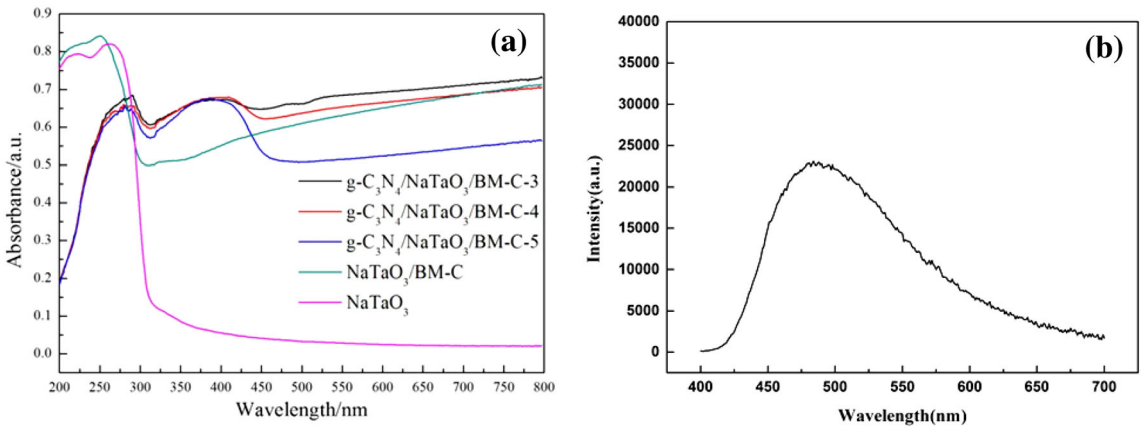

Fig. 5 UV–vis diffuses reflectance spectra of the $NaTaO_3$, $NaTaO_3$/BM-C, g-C_3N_4/$NaTaO_3$/BM-C composites (**a**), PL emission spectra of g-C_3N_4/$NaTaO_3$/BM-C photocatalyst (**b**)

4 Photocatalytic activity of the g-C_3N_4/$NaTaO_3$/BM-C

Before illumination, the as-prepared photocatalysts were continuously stirred in a dark room for 60 min to achieve adsorption–desorption equilibrium, the adsorption properties of which were discussed as shown in Fig. 7a. It can be seen that the g-C_3N_4/$NaTaO_3$/BM-C showed excellent adsorption performance. Among them, the adsorption extent of g-C_3N_4/$NaTaO_3$/BM-C-5 reached 56.69%, and the adsorption capacity increased slightly with the increase of melamine content. The photocatalytic activity of the as-prepared g-C_3N_4/$NaTaO_3$/BM-C photocatalysts was further evaluated by photocatalytic degradation of Rh B as a model reaction under visible-light irradiation. The results are shown in Fig. 7b. For comparison, the photocatalytic activities of pure g-C_3N_4, g-C_3N_4/$NaTaO_3$, and $NaTaO_3$/BM-C were also tested under identical experimental conditions. The concentration of Rh B solution in the blank test changed little, indicating that irradiation without the photocatalyst has little effect on the degradation process. After 60 min of visible-light illumination, the photocatalytic conversion extents of Rh B for pure g-C_3N_4, g-C_3N_4/$NaTaO_3$, $NaTaO_3$/BM-C, and g-C_3N_4/$NaTaO_3$/BM-C-4 were 32.21%, 44.87%, 54.39%, and 95.85%, respectively. Remarkably, the photocatalytic activity of g-C_3N_4/$NaTaO_3$/BM-C composite was much higher than that of $NaTaO_3$/BM-C and g-C_3N_4/$NaTaO_3$. This confirmed that the presence of g-C_3N_4 could facilitate the visible-light catalytic activity of $NaTaO_3$/BM-C. Subsequently, it was noted that the photocatalytic activity of g-C_3N_4/$NaTaO_3$/BM-C was significantly improved as the amount of melamine added increased. This result clearly showed that there existed a significant synergistic effect between g-C_3N_4 and $NaTaO_3$/BM-C for photocatalytic degradation of Rh B under visible-light irradiation. Because the mass ratio of melamine to binary $NaTaO_3$/BM-C is 4:1, the composite photocatalytic material exhibited the highest visible-light catalytic activity. Nevertheless, when the mass ratio of melamine to binary $NaTaO_3$/BM-C continued to increase, the photocatalytic activity of the composite was decreased. This is mainly because the excess g-C_3N_4 covering the surface of $NaTaO_3$/BM-C decreased the synergistic effect between g-C_3N_4 and $NaTaO_3$/BM-C. On the one hand, the adsorption active site of the BM-C in the material system is covered, thus limiting the adsorption performance. On the other hand, a large component of g-C_3N_4 disrupted the transport separation of charge carriers, resulting in a decrease in photocatalytic activity. In a word, the g-C_3N_4/$NaTaO_3$/BM-C has eminent visible-light catalytic performance.

It is known from previous reports that the photocatalytic degradation of Rh B follows first-order kinetics, and the integrated rate law of the first-order kinetic model can be expressed as follows:

$$-\ln(C_t/C_0) = kt, \tag{4}$$

where C_t is the concentration at time t, C_0 is the initial dye concentration in solution, k is the first-order rate constant, and t is the illumination time. As presented

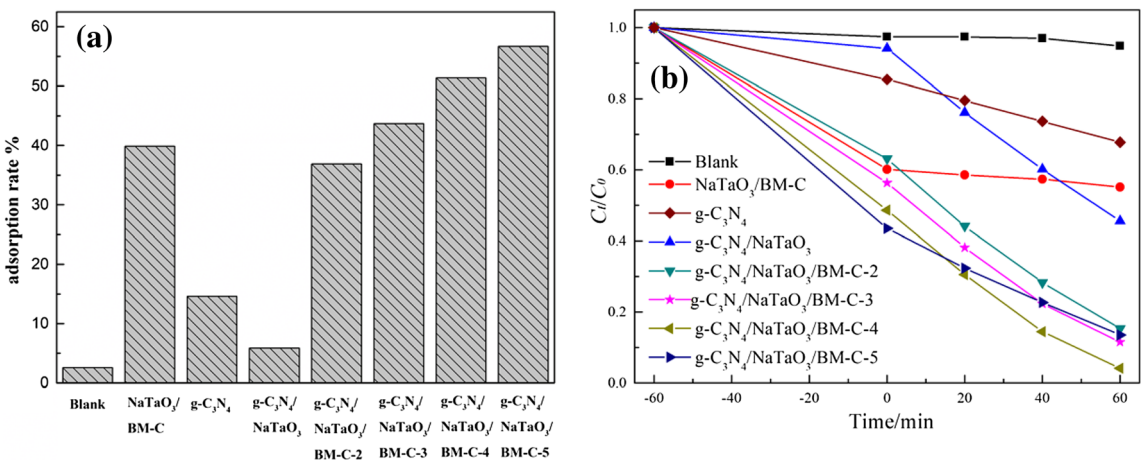

Fig. 7 Photocatalytic activity of g-C_3N_4/$NaTaO_3$/BM-C composites on degrading RhB (**a**), and the adsorption rates of all samples in adsorption–desorption equilibrium after continuous stirring for 60 min under dark room conditions (**b**)

in Fig. 8, the first-order rate constants over $NaTaO_3$/BM-C, g-C_3N_4/$NaTaO_3$, and g-C_3N_4/$NaTaO_3$/BM-C-4 are 0.0014, 0.0133, and 0.0407 min^{-1} for degradation of Rh B, respectively. The results clearly demonstrate that the photocatalytic capacity of g-C_3N_4/$NaTaO_3$/BM-C-4 has reached optimum under visible-light illumination, which is superior to $NaTaO_3$/BM-C and g-C_3N_4/$NaTaO_3$. Furthermore, the radicals and holes trapping experiments were carried out at the same time to identify the reactive species of the degradation process. Isopropyl alcohol (IPA), ammonium oxalate (AO), and benzoquinone (BQ) were employed as the scavenger of hydroxyl radicals (•OH), photogenerated holes (h^+), and superoxide radicals ($•O_2^-$), respectively. The result demonstrates that superoxide radicals play a major role in the reaction system.

Based on the above experimental results, a possible photocatalytic mechanism of the g-C_3N_4/$NaTaO_3$/BM-C photocatalyst is proposed, as shown in Fig. 9. Under visible-light irradiation, the photogenerated electrons in the CB of the g-C_3N_4 injected directly into that of $NaTaO_3$, which led to the accumulation of holes on the surface of g-C_3N_4, effectively inhibiting the recombination of electrons and holes. Because the CB edge potential of $NaTaO_3$ (− 0.773 eV) was more negative than the reduction potential of O_2 to $•O_2^-$ radical, the electrons accumulated in the CB of $NaTaO_3$ could be transferred to the surface of BM-C and $•O_2^-$ formed. As a strong oxidizing substance, superoxide radicals $•O_2^-$ were able to promote the oxidative degradation of Rh B and other organic pollutants. At the same time, the oxidation reaction of

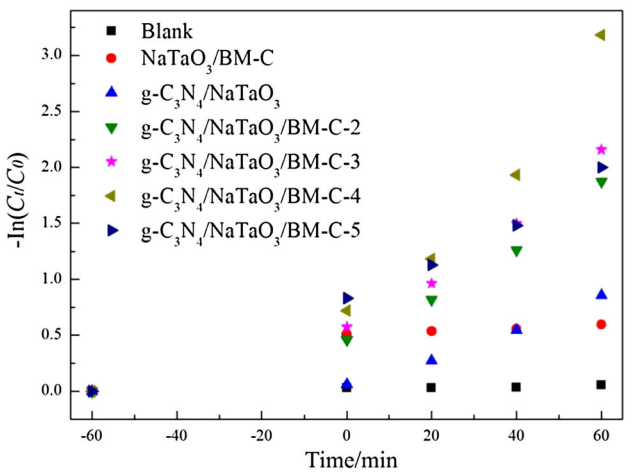

Fig. 8 Kinetic fit for the photodegradation of RhB by g-C_3N_4/$NaTaO_3$/BM-C composites

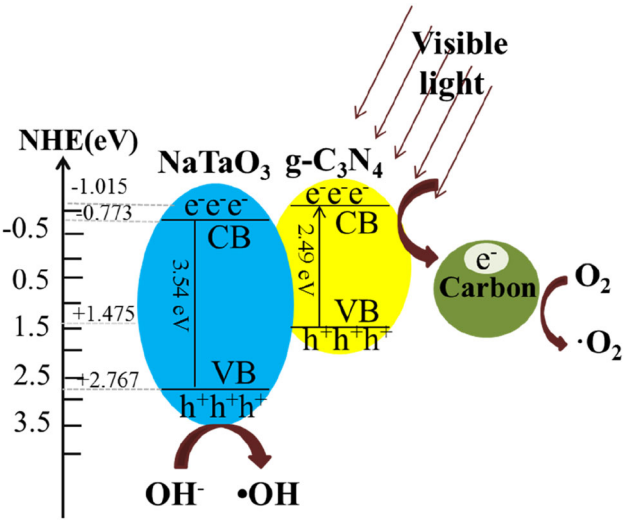

Fig. 9 Photocatalytic mechanism of the g-C_3N_4/$NaTaO_3$/BM-C composites

the holes h^+ of $NaTaO_3$ could oxidize organic dyes directly. Moreover, dyes could be absorbed by BM-C, thus could assist the degradation of Rh B. As a result, dramatic photocatalytic activity is generated over g-C_3N_4/$NaTaO_3$/BM-C hybrid nanocomposite under proper experimental conditions.

5 Conclusions

In summary, we have successfully synthesized visible-light-responsive g-C_3N_4/$NaTaO_3$/BM-C nanocomposites through a solvothermal method combined with a high-temperature sintering method. The addition of melamine (the g-C_3N_4 precursor) has been demonstrated to have a significant influence on the morphology, composition, and photocatalytic activity of the composite. In this ternary composite structure, the good synergistic effect between g-C_3N_4 and $NaTaO_3$ can effectively promote the migration efficiency of photoinduced electron–hole pairs. The introduction of BM-C can accelerate the electron-transfer rate and expand the range of light absorption, enhancing photocatalytic activity. The photocatalytic activity test of the composites revealed that the g-C_3N_4/$NaTaO_3$/BM-C composite showed the highest photocatalytic activity when the mass ratio of melamine to binary $NaTaO_3$/BM-C is 4:1, and the degradation extent of Rh B reached 95.85% in 60 min under visible-light irradiation. Compared with $NaTaO_3$/BM-C and g-C_3N_4/$NaTaO_3$, the

degradation extent of g-C_3N_4/$NaTaO_3$/BM-C composite increased by 73% and 66.86%, respectively. Overall, this work provides useful insights for promoting the practical process of sodium tantalate photocatalytic materials.

Acknowledgements

This research work was supported by the Natural Science Foundation of Zhejiang Province, China (Grant No. LY19E030009), and the Fundamental Research Funds of Zhejiang Sci-Tech University (Grant No. 2019Q009).

References

1. R. Ameta, D. Soni, S. Benjamin, N. Chouhan, S.C. Ameta, Mater. Sci. Forum **855**, 58 (2016)
2. N.Y. Liu, M. Han, Y. Sun, C. Zhu, Y.J. Zhou, Y.L. Zhang, H. Huang, V. Kremnican, Y. Liu, Y. Lifshitz, Z.H. Kang, Energy Environ. Sci. **11**(7), 1841 (2018)
3. L. Long, E. Yang, X. Qi, R. Xie, Z. Bai, S. Qin, C. Deng, W. Zhong, ACS Sustain. Chem. Eng. **8**(1), 613 (2020)
4. Y.J. Yuan, D. Chen, Z.T. Yu, Z.G. Zou, J. Mater. Chem. A **6**(25), 11606 (2018)
5. H. Liu, S.J. Chang, Y.H. Sang, X.Q. Yang, Chem Asian J. **11**(17), 2352 (2016)
6. H.R. Han, X. Qian, Y. Yuan, M. Zhou, Y.L. Chen, Water Air Soil Pollut. **227**(12), 461 (2016)
7. M. Motola, M. Caplovicova, M. Krbal, H. Sopha, G.K. Thirunavukkarasu, M. Gregor, G. Plesch, J.M. Macak, Electrochim. Acta **331**, 135374 (2020)
8. Q.Y. Wang, H.L. Li, X.L. Yu, Y. Jia, Y. Chang, S.M. Gao, Electrochim. Acta **330**, 135167 (2020)
9. M. Mondal, H. Dutta, S.K. Pradhan, Mater. Chem. Phys. **248**, 122947 (2020)
10. M.R. Al-Mamun, S. Kader, M.S. Islam, M.Z.H. Khan, J. Environ. Chem. Eng. **7**, 103248 (2019)
11. G.R. Portugal, S.F. Santos, J.T. Arantes, Appl. Surf. Sci. **502**, 144206 (2020)
12. L. Tang, C.Y. Feng, Y.C. Deng, G.M. Zeng, J.J. Wang, Y. Liu, H.P. Feng, J.J. Wang, Appl. Catal. B Environ. **230**, 102 (2018)
13. M. Zhang, G.H. Liu, D.Z. Zhang, Y. Chen, S.P. Wen, S.P. Ruan, J. Alloys Compd. **602**, 322 (2014)
14. F.F. Li, D.R. Liu, G.M. Gao, B. Xue, Y.S. Jiang, Appl. Catal. B Environ. **166–167**, 104 (2015)
15. S.J. Li, H. Qiu, C.D. Wang, Y.F. Sun, X.S. Du, J.Y. Zhao, Sol. Energy Mater. Sol. Cells **149**, 97 (2016)
16. J. Zhang, D.M. Zhang, Can. J. Phys. **98**(3), 233 (2020)
17. H. Li, X.B. Shi, X.G. Liu, X. Li, Appl. Surf. Sci. **508**, 145306 (2020)
18. Y.L. Liu, C.L. Yang, M.S. Wang, X.G. Ma, Y.G. Yi, Mater. Res. Bull. **107**, 125 (2018)
19. I. Ivanova, T.A. Kandiel, Y.J. Cho, W.Y. Choi, D. Bahnemann, ACS Catal. **8**, 2313 (2018)
20. A. Malankowska, M.P. Kobylański, A. Mikolajczyk, O. Cavdar, G. Nowaczyk, M. Jarek, W. Lisowski, M. Michalska, E. Kowalska, B. Ohtani, A. Zaleska-Medynska, ACS Sustain. Chem. Eng. **6**(12), 16665 (2018)
21. C.X. Lu, Y. Chen, Y. Li, C.H. Ma, Y.W. Guo, Y. Li, J. Wang, Energy **93**, 749 (2015)
22. D.B. Xu, L.L. Li, H.M. Xu, J.J. Zhu, W.Q. Fan, J.R. Ding, W.D. Shi, J. Solid State Chem. **280**, 120986 (2019)
23. J.M. Mora-Hernandeza, A.M. Huerta-Flores, L.M. Torres-Martínez, J. Photochem. Photobiol. A Chem. **391**, 112363 (2020)
24. S. Wang, X.W. Xu, H. Luo, C.C. Cao, X.Y. Song, J.L. Zhao, J. Zhang, C.C. Tang, RSC Adv. **8**, 19279 (2018)
25. J.M. Mora-Hernandez, A.M. Huerta-Flores, L.M. Torres-Martínez, J. Photochem. Photobiol. A Chem. **391**, 112363 (2020)
26. D. Masih, Y.Y. Ma, S. Rohani, Appl. Catal. B Environ. **206**, 556 (2017)
27. F.L. Yang, F.F. Xia, J. Hu, C.Z. Zheng, J.H. Sun, H.B. Yi, RSC Adv. **8**, 1899 (2018)
28. Q.L. Xu, B.C. Zhu, B. Cheng, J.G. Yu, M.H. Zhou, W.K. Ho, Appl. Catal. B Environ. **255**, 117770 (2019)
29. J. Fu, J. Yu, C. Jiang, B. Cheng, Adv. Energy Mater. **8**(3), 1701503 (2017)
30. A. Mishra, A. Mehta, S. Basua, N.P. Shetti, K.R. Reddy, T.M. Aminabhavi, Carbon **149**, 693 (2019)
31. R. Wang, E. Yang, X. Qi, R. Xie, S. Qin, C. Deng, W, Zhong. Appl. Surf. Sci. **516**, 146159 (2020)
32. G.X. Zhang, Y.M. Chen, Y.G. Chen, H.B. Guo, Mater. Res. Bull. **102**, 391 (2018)
33. X.X. Zhao, Z.Y. Lu, R. Ji, M.H. Zhang, C.W. Yi, Y.S. Yan, Catal. Commun. **112**, 49 (2018)
34. A. Sandoval, H.V. Cristina, T.E. Klimova, Fuel **198**, 22 (2017)
35. M. Vinayagam, S. Ramachandran, V. Ramya, A. Sivasamy, J. Environ. Chem. Eng. **6**(3), 3726 (2018)
36. F.Y. Cai, Y.Q. Zhang, J.T. Wang, J.R. Zhou, H.L. Cao, J. Lü, Environ. Sci. Pollut. Res. **26**, 31055 (2019)
37. Y. Yu, Z. Zhu, Z. Liu, H.J. Dong, Y. Liu, M.B. Wei, P.W. Huo, C.X. Li, Y.S. Yan, J. Taiwan Inst. Chem. E. **102**, 197 (2019)
38. S. Suzuki, H. Wagarta, K. Yubuta, S. Oishi, K. Teshima, CrystEngComm **17**(47), 9016 (2015)

39. A. Maavia, I. Aslam, M. Tanveer, M. Rizwan, M.W. Iqbal, M. Tahir, H. Hussain, R. Boddula, M. Yousuf, Mater. Sci. Energy Technol. **2**(2), 258 (2019)
40. N. Tian, H. Huang, Y. He, Y. Guo, Y. Zhang, RSC Adv. **4**(80), 42716 (2014)
41. J.W. Fu, Q.L. Xua, J.X. Low, C.J. Jiang, J.G. Yu, Appl. Catal. B Environ. **243**, 556 (2019)
42. F.L. Wang, Y.F. Wang, Y.P. Feng, Y.Q. Zeng, Z.J. Xie, Q.X. Zhang, Y.H. Su, P. Chen, Y. Liu, K. Yao, W.Y. Lv, G.G. Liu, Appl. Catal. B Environ. **221**, 510 (2018)
43. C.H. Chien, Y.H. Chang, C.P. Tsai, C.W. Peng, L.S. Wang, P.S. Sheng, C.Y. Lee, H.T. Chiu, J. Chin. Chem. Soc. **53**(2), 287 (2013)
44. D.F. Xu, B. Cheng, W.K. Wang, C.J. Jiang, J.G. Yu, Appl. Catal. B Environ. **231**, 368 (2018)
45. C.C. Han, L. Ge, C.F. Chen, Y.J. Li, X.L. Xiao, Y.N. Zhang, L.L. Guo, Appl. Catal. B Environ. **147**(1–2), 546 (2014)
46. S. Kumar, B. Kumar, T. Surendar, V. Shanker, Mater. Res. Bull. **49**, 310 (2014)
47. F. Yang, L.N. Yan, B. Zhang, X. He, Y. Li, Y.S. Tang, C. Ma, Y.F. Li, J. Alloys Compd. **805**, 802 (2019)